Non-Hermitian Zitterbewegung Effect

Jiahao Wu(吴嘉豪)[1,2], Han-Jie Zhu(朱汉杰)[3], and Wu-Ming Liu(刘伍明)[1*]

[1] Beijing National Laboratory for Condensed Matter Physics,

and Institute of Physics, Chinese Academy of Sciences, Beijing 100190, China

[2] School of Physical Sciences, University of Chinese Academy of Sciences, Beijing 100049, China

[3] Center for Joint Quantum Studies and Department of Physics.School of Science,Tianjin University,Tianjin,300350,China

October 3, 2026

Abstract

We investigate the general form of the Zitterbewegung (ZB) effect in non-Hermitian systems for a multi-band Hamiltonian depending on momentum, where the ZB effect is the multifrequency oscillatory motion of the quasiparticle. We propose a real non-Hermitian Luttinger Hamiltonian that describes holes near the top of the valence band in common zinc-blende and diamond-structured semiconductors (GaAs, Si, Ge, etc.) and enables the observation of the ZB effect. By evaluating the dynamical evolution of light and heavy holes, we demonstrate that non-Hermiticity acts as an amplifier for ZB oscillations. This amplification, rooted in the complex energy spectrum, allows us to predict the maximal enhancement of transient ZB oscillations within the short-time physical window. An experimental scheme is proposed to observe the ZB effect by measuring the motion of the holes. Our findings offer a new perspective on the transport properties of open quantum systems and semiconductor carrier transport.

Keywords: non-Hermitian physics, Luttinger Hamiltonian, semiconductor, Zitterbewegung effect

PACS: 03.65.Yz, 71.70.Ej, 72.20.Jv, 78.47.J-

1. Introduction

In 1930, Schrödinger predicted the ZB effect which is a rapid "trembling motion" of electrons through the Dirac equation [1]. He attributed this oscillation to the interference between positive and negative energy states, with an amplitude on the order of the Compton wavelength, making direct experimental observation extremely challenging. However, ZB is not confined to relativistic systems, it has been identified in semiconductors [2–9], ultracold atomic systems [10,11] and waveguide arrays [12–14] etc. More generally, ZB oscillations emerge in any system characterized by multiple energy bands [15]. To date, ZB phenomena in Hermitian systems have been extensively investigated [15–22]. Early research focused primarily on Hermitian systems, where the Hamiltonians correspond to real energy eigenvalues. Non-Hermitian physics was revolutionized by

*Corresponding authors. E-mail: 256176@tju.edu.cn; wmliu@iphy.ac.cn

the discovery that non-Hermitian Hamiltonians can also possess real spectra under certain symmetries [23]. Furthermore, non-Hermitian systems are inherently linked to open environments, sparking a surge of interest in non-Hermitian physics [24–31]. Deepening research has unveiled novel phenomena unique to non-Hermitian systems, such as non-Hermitian skin effect [32], generalized Brillouin zone [33] and other non-Hermitian topological properties [34,35], exceptional points and exceptional lines [36,37], scattering paths [38]. Unlike their Hermitian counterparts, the eigenstates of non-Hermitian Hamiltonians do not form an orthogonal basis but instead satisfy the biorthogonal normalization condition [39], which is characterized by left and right eigenstates.

Despite these advancements, studies on ZB in non-Hermitian frameworks remain scarce, though preliminary investigations have hinted at its unique nature [40–47]. Specifically, since non-Hermitian eigenvalues contain imaginary components, the ZB oscillation amplitude can undergo dramatic modifications [46]. Moreover, governed by biorthogonality, wave packets in non-Hermitian systems exhibit oscillation terms absent in Hermitian cases [44]. A cornerstone for studying ZB is the Luttinger Hamiltonian [48], which describes four states near the top of the valence band, with twofold light-hole and heavy-hole states. Ge's approximate energy band is presented in Fig. 1. The valence band of heavy holes (VBHH) is higher than that of valence band of light holes (VBLH) and a large number of electrons occupy the energy bands [Fig. 1(a)]. In the Hermitian Luttinger model, ZB is manifest as a quantum mechanical oscillation [15]. As we demonstrated in our previous work [49], applying a dc electric field induces observable semiclassical ZB oscillations. The physical origin of this emergence can be attributed to the transverse spin force exerted on the spin current under an electric field [50]. Building upon our foundational investigation of these carrier dynamics [49], the present study generalizes our theoretical framework to open, driven-dissipative systems from non-Hermitian perspective.

In this work, we extend the theory of ZB to a generalized non-Hermitian framework for a multiband Hamiltonian depending on momentum. Specifically, we construct an effective non-Hermitian Luttinger Hamiltonian with holes that would gain or lose energy in an open, driven-dissipative system. We demonstrate that non-Hermiticity, arising from interband scattering, acts as a significant amplifier for ZB oscillations. This amplification is rooted in the interplay between the complex energy spectrum. Crucially, by restricting our exact non-Hermitian dynamics strictly to the picosecond coherent window, we demonstrate that this mechanism provides a viable theoretical pathway to exponentially amplify and experimentally detect transient ZB oscillations before continuous scattering completely dismantles the quantum interference. We further propose an experimentally feasible realization. Our findings offer a new perspective on the transport properties of open quantum systems and the ultrafast dynamics of semiconductor carriers.

2. Theoretical derivation of non-Hermitian ZB effect

In contrast to the standard Hermitian Luttinger model which describes a closed equilibrium system, our setup involves an open quantum environment driven by optical pumping. Photons of specific energy can drive interband transitions within the valence bands while leaving the conduction-valence gap intact. Here, electrons in the VBLH are scattered by photons and then gain energy, triggering them to transit to the VBHH [Fig. 1(b)]. Since the VBHH resides at a higher energy compared to the VBLH, the optical pumping drives a continuous interband transition of electrons from the lower to the upper band. This selective optical transition fundamentally breaks the detailed balance of the system. From a phenomenological perspective of hole dynamics,

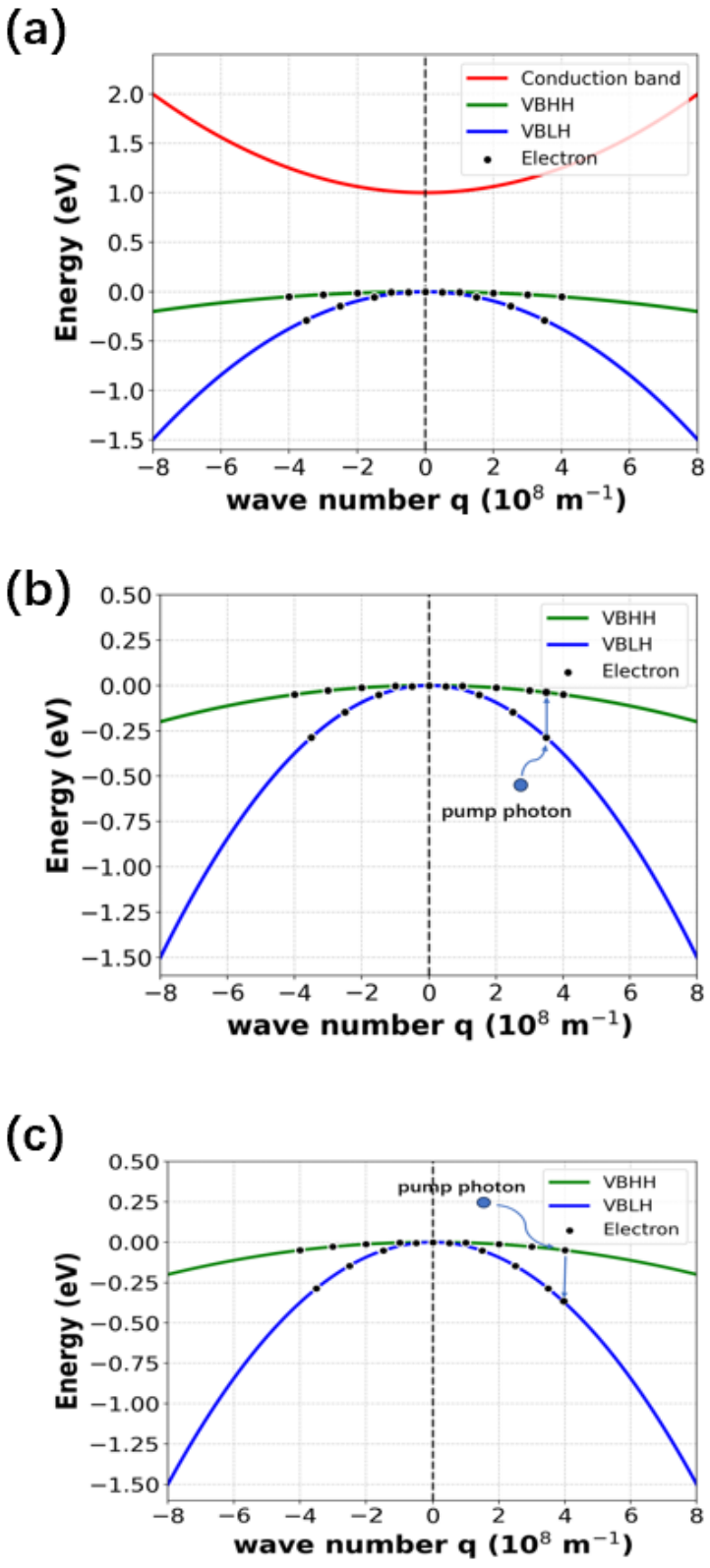


Figure 1: Schematic of band structure and interband scattering processes between valence bands; taking Ge as a representative case. (a) Approximate band structure of Ge. The upper band is the valence band of heavy holes, the lower band is the valence band of the light holes. (b) Photon drives electrons from the lower to the upper band. (c) Photon drives electrons from the upper to the lower band.

the continuous extraction of electrons from the VBLH creates a surplus of vacancies (acting as an effective gain for light holes), while the accumulation of electrons in the VBHH leads to a rapid depletion (acting as an effective loss for heavy holes). This microscopic asymmetry in carrier lifetimes naturally breaks the Hermitian symmetry, driving the system into a non-equilibrium state characterized by finite quasiparticle lifetimes.

Under this condition, we introduce a non-Hermitian Hamiltonian in momentum space.

$$H = \frac{1}{2m}[(\gamma_1 + \frac{5}{2}\gamma_2)k^2 - 2\gamma_2(\mathbf{k}\cdot\mathbf{S})^2] + H_{loss}, \tag{1}$$

where $\mathbf{k}$ denotes the physical momentum, γ_1 and γ_2 are dimensionless Luttinger parameters characterizing the semiconductor material, and $\mathbf{S} = (S_x, S_y, S_z)$ is the vector of 4×4 spin-3/2 operator matrices. The explicit representations of these matrices are provided in Appendix A. We define the purely imaginary non-Hermitian term as:

$$H_{loss} = \begin{pmatrix} i\kappa & 0 & 0 & 0 \\ 0 & -i\kappa & 0 & 0 \\ 0 & 0 & -i\kappa & 0 \\ 0 & 0 & 0 & i\kappa \end{pmatrix}, \tag{2}$$

where κ is the phenomenological non-Hermitian coefficient. Physically, the non-Hermitian term H_{loss} models an externally engineered, band-selective mechanism (distinguishing heavy hole and light hole) that preserves spin degeneracy. Because this external driving effectively couples to the squared projection of the angular momentum in the fixed spatial frame rather than the internal carrier momentum space, the operator is intrinsically diagonal and spin-degenerate in the m_J basis. A detailed mathematical proof demonstrating how this fixed-basis operator perturbatively maps onto the momentum-dependent heavy-hole and light-hole energy bands is provided in Appendix C. Its right eigenstates $|\psi_n\rangle$ and left eigenstates $|\phi_n\rangle$ satisfy

$$H|\psi_n\rangle = E_n|\psi_n\rangle, H^\dagger|\phi_n\rangle = E_n^*|\phi_n\rangle. \tag{3}$$

They obey the biorthogonality condition $\langle u_m|\psi_n\rangle = \delta_{mn}$ and the completeness relation $\sum_n |u_n\rangle\langle\phi_n| = I$, the projection operator is defined as $Q_n = |u_n\rangle\langle\phi_n|$, where $|u_n\rangle$ is defined in Appendix A. The energy spectrum for light holes (ϵ_L) and heavy holes (ϵ_H) is

$$\epsilon_{L/H} = \frac{k^2\gamma_1 \pm 2\sqrt{k^4\gamma_2^2 + im\gamma_2(k^2 - 3k_z^2) - m^2\kappa^2}}{2m}. \tag{4}$$

Here, we introduce the approximation $m^2\kappa^2 \ll k^4\gamma_2^2$ and expand the energy to the first order which gives

$$\epsilon_{L/H} = \frac{k^2\gamma_1 \pm 2k^2\gamma_2 \pm \frac{im\kappa(k^2 - 3k_z^2)}{k^2\gamma_2}}{2m}. \tag{5}$$

We note that under this condition, the system operates in a perturbative regime where the term inside the square root of Eq. (4) remains non-zero. Consequently, no EPs emerge in our considered parameter space. This is physically justified, as κ induced by carrier scattering is significantly smaller than the kinetic energy scale of the bands. If the non-Hermitian coefficient were to drastically increase such that $m_0^2\kappa^2 \sim k^4\gamma_2^2$, EPs would emerge. Our study focuses on the physically accessible regime far from EPs.

The evolution of the position operator in the Heisenberg picture follows [51]

$$O(t) = U^{-1}(t, t_0)O(t_0)U(t, t_0), \tag{6}$$

where $U(t,t_0) = e^{-iH(t-t_0)/\hbar}$ is the time evolution operator. We need clarify that in the standard Hermitian regime, the evolution of an observable O is given by $O(t) = U^\dagger O(0) U$. However, in a non-Hermitian system where $H \neq H^\dagger$, the relation $U^{-1} = U^\dagger$ no longer holds. According to the non-Hermitian Schrödinger equation, the right state evolves as $i\hbar\frac{\partial}{\partial t}|\psi(t)\rangle_R = H|\psi(t)\rangle_R$, which yields $|\psi(t)\rangle_R = U(t,t_0)|\psi(t_0)\rangle_R$. The Hermitian conjugate yields $-i\hbar\frac{\partial}{\partial t}{}_R\langle\psi(t)| =_R \langle\psi(t)|H^\dagger$, meaning ${}_R\langle\psi(t)| =_R \langle\psi(t_0)|U^\dagger(t,t_0)$. While the conventional right-state Dirac inner product effectively evaluates macroscopic observables in open systems, analytically decoupling the ZB effect makes it highly advantageous to employ the biorthogonal basis. The corresponding left state satisfies ${}_L\langle\phi_n|H = E_L\langle\phi|$, and its time evolution is governed by $-i\hbar\frac{\partial}{\partial t}{}_L\langle\psi(t)| =_L \langle\psi(t)|H$, leading to ${}_L\langle\psi(t)| =_L \langle\psi(t_0)|U^{-1}(t,t_0)$. Therefore, to maintain the consistency of the biorthogonal inner product, the generalized Heisenberg representation requires the operator to evolve as $O(t) = U^{-1}OU$, demonstrating that $O(t) \neq U^\dagger OU = e^{iH^\dagger(t-t_0)/\hbar}Oe^{-iH(t-t_0)/\hbar}$ in the non-Hermitian framework. The position operator evolves as

$$\begin{aligned}\mathbf{x}(t) &= U^{-1}\mathbf{x}(0)U \\ &= U^{-1}[\mathbf{x}(0), U] + U^{-1}U\mathbf{x}(0) \\ &= \mathbf{x}(0) + i\hbar U^{-1}\frac{\partial U}{\partial \mathbf{k}}.\end{aligned} \tag{7}$$

We can expand time evolution operator in terms of projection operator as $U = e^{-iHt/\hbar} = \sum_a e^{-iE_a t/\hbar}Q_a$, then Eq. (7) becomes

$$\mathbf{x}(t) = \mathbf{x}(0) + \mathbf{Z}_{aa} + t\sum_a \mathbf{V}_a Q_a + \sum_a\sum_{a\neq b}\mathbf{Z}_{ab}e^{i\omega_{ab}t}, \tag{8}$$

where $V_a = \frac{\partial E_a}{\partial \mathbf{k}}$,$\mathbf{Z}_{ab} = i\hbar Q_a\frac{\partial Q_b}{\partial \mathbf{k}}$ and $\omega_{ab} = \frac{E_a - E_b}{\hbar}$. $\mathbf{V}_a$ denotes the particle's velocity of normal motion behavior, $\mathbf{Z}_{ab}$ denotes the ZB amplitude of the particle. ω_{ab} is called beating frequency, which means the energy difference of different bands. Eq. (8) is formally identical to the Hermitian expression, though the operators differ. We emphasize the fundamental physical necessity of this biorthogonal evaluation. In a Hermitian system with orthogonal eigenstates, separating the macroscopic semiclassical drift from the microscopic ZB oscillations is mathematically trivial. However, in our non-Hermitian framework, the right eigenstates are intrinsically non-orthogonal. If the expectation value were evaluated using the conventional right-state Dirac inner product, the interband cross-terms could not be algebraically eliminated, leaving the drift and ZB oscillations inextricably entangled. The biorthogonal formalism intrinsically resolves this issue by restoring the resolution of identity. This mathematical restoration is precisely what enables the clean and rigorous decomposition in Eq. (8) into an uncoupled constant drift and an oscillatory ZB interference.

For the Luttinger Hamiltonian, which has only two energy levels, the oscillation frequency is unique. Its Hamiltonian can be written in terms of projection operator $H = \epsilon_L Q_L + \epsilon_H Q_H$. For convenient calculation, assuming the momentum along the z axis is much less than the momentum along the other two axes. Here, we assume that the momentum along the z axis is one order less than the x and y axes. The result is similar to Hermitian case [15].

$$\mathbf{x}(t) = \mathbf{x}(0) + \mathbf{W}t + \mathbf{Z}(t), \tag{9a}$$

$$\mathbf{W} = \frac{\partial\varepsilon}{\partial\mathbf{k}}I + \frac{1}{2}\frac{\partial\hbar\omega}{\partial\mathbf{k}}\mathbf{T}, \tag{9b}$$

$$\mathbf{Z}(t) = \frac{\hbar}{2}sin(\omega t)\frac{\partial\mathbf{T}}{\partial\mathbf{k}} + \frac{\mathrm{i}\hbar}{2}[1-\cos(\omega t)]T\frac{\partial T}{\partial\mathbf{k}}., \tag{9c}$$

where $T = Q_L - Q_H, \varepsilon = (\epsilon_L + \epsilon_H)/2 = \frac{k^2\gamma_1}{2m}, \omega = (\epsilon_L - \epsilon_H)/\hbar = \frac{2k^2\gamma_2}{m\hbar} + \frac{i\kappa}{\gamma_2\hbar} - \frac{3i\kappa k_z^2}{k^2\gamma_2\hbar}$. Projection operators Q_L and Q_H are (for detailed derivation, see the Appendix A):

$$\begin{aligned} Q_L =& \left(\frac{\boldsymbol{\beta}}{2k^2} - \frac{1}{8}I_4\right)\left(1 - \frac{im\kappa}{2k^2\gamma_2} + \frac{3k_z^2}{2k^2}\frac{im\kappa}{k^2\gamma_2}\right) \\ &- \frac{3k_z^2}{4k^2}\frac{im\kappa}{k^2\gamma_2}I_4 - \frac{4S_z^4 + S_z^2 - 17I_4}{22}\frac{im\kappa}{k^2\gamma_2}, \end{aligned} \tag{10a}$$

$$\begin{aligned} Q_H =& \left(\frac{\boldsymbol{\beta}}{2k^2} - \frac{1}{8}I_4\right)\left(\frac{im\kappa}{2k^2\gamma_2} - \frac{3k_z^2}{2k^2}\frac{im\kappa}{k^2\gamma_2}\right) + \frac{9}{8}I_4 \\ &- \frac{\boldsymbol{\beta}}{2k^2} + \frac{4S_z^4 + S_z^2 - 17I_4}{22}\frac{im\kappa}{k^2\gamma_2} \\ &+ \frac{3k_z^2}{4k^2}\frac{im\kappa}{k^2\gamma_2}I_4. \end{aligned} \tag{10b}$$

From Eqs. (10a) and (10b), the expression of operator T is given by

$$\begin{aligned} T =& \frac{5}{4}I_4 - \frac{\boldsymbol{\beta}}{k^2} + \frac{3k_z^2}{2k^2}\frac{im\kappa}{k^2\gamma_2}I_4 \\ &+ \left(\frac{\boldsymbol{\beta}}{2k^2} - \frac{1}{4}I_4\right)\left(\frac{im\kappa}{2k^2\gamma_2} + \frac{3k_z^2}{2k^2}\frac{im\kappa}{k^2\gamma_2}\right) \\ &+ \frac{4S_z^4 + S_z^2 - 17I_4}{22}\frac{im\kappa}{k^2\gamma_2}. \end{aligned} \tag{11}$$

We first consider κ as a constant, then

$$\frac{\partial\hbar\omega}{\partial\mathbf{k}} = \frac{4\mathbf{k}\gamma_2}{m} - \frac{3i\kappa}{\gamma_2}\left(\frac{2\boldsymbol{k_z}\frac{\partial\boldsymbol{k_z}}{\partial\mathbf{k}}k^2 - 2k_z^2\mathbf{k}}{k^4}\right), \tag{12a}$$

$$\begin{aligned} \frac{\partial T}{\partial\mathbf{k}} =& \frac{2\mathbf{k}\boldsymbol{\beta}}{k^4} + \frac{im\kappa}{2\gamma_2}\frac{\boldsymbol{\alpha}k^2 - 4\boldsymbol{\beta}\mathbf{k}}{k^6} - \frac{\boldsymbol{\alpha}}{k^2} \\ &+ \frac{im\kappa\mathbf{k}}{2\gamma_2 k^4}I_4 - \frac{4S_z^4 + S_z^2 - 17I_4}{11}\frac{im\kappa}{k^2\gamma_2}\frac{2\mathbf{k}}{k^2} \\ &- \frac{3im\kappa}{2\gamma_2}\frac{(\boldsymbol{\alpha}k_z^2 + 2\boldsymbol{\beta}\boldsymbol{k_z}\frac{\partial\boldsymbol{k_z}}{\partial\mathbf{k}})k^2 - 6\boldsymbol{\beta}k_z^2\mathbf{k}}{k^8} \\ &+ \frac{15im\kappa}{8\gamma_2}\frac{2\boldsymbol{k_z}\frac{\partial\boldsymbol{k_z}}{\partial\mathbf{k}}k^2 - 4k_z^2\mathbf{k}}{k^6}, \end{aligned} \tag{12b}$$

where $\boldsymbol{\alpha} = \mathbf{S}(\mathbf{k}\cdot\mathbf{S}) + (\mathbf{k}\cdot\mathbf{S})\mathbf{S}, \boldsymbol{\beta} = (\mathbf{k}\cdot\mathbf{S})^2$.

3. Dynamical evolution under various non-Hermitian scenarios

3.1. Dynamics under constant non-Hermitian coupling

We take the semiconductor Ge as an example, whose semiconductor parameters $\gamma_1 \approx 13.2$, $\gamma_2 \approx 5$ [48]. The order of the wave number is about $10^8\ m^{-1}$ [52]. Therefore, setting the initial position $\mathbf{x}(0) = 0$, the initial wave vectors satisfy $|\mathbf{q}_{\mathbf{x}_0}| = \frac{k_{x0}}{\hbar} = 2.82 \times 10^8\ m^{-1}$, $|\mathbf{q}_{\mathbf{y}_0}| = 2.82 \times 10^8\ m^{-1}$, $|\mathbf{q}_{\mathbf{z}_0}| = 0.31 \times 10^8\ m^{-1}$ (the total wave number $q_0 = 4 \times 10^8\ m^{-1}$) and choosing $\kappa = \frac{6}{1000}\frac{k_0^2}{m}$. In our numerical simulations, the system is initialized at $t = 0$ using a specifically tailored wave packet. This initial state is a coherent superposition of heavy holes (HH) and light holes (LH) , expressed generally as $|\Psi\rangle = c_1|\psi_{HH}\rangle + c_2|\psi_{LH}\rangle$ (and analogously for the left state $\langle\Phi| = c_1\langle\phi_{HH}| + c_2\langle\phi_{LH}|$). Depending on the specific dynamics being investigated, the wave packet is prepared such that one component heavily dominates. For instance, when analyzing HH-dominated dynamics, we set $|c_1| \gg |c_2|$. The dominant HH left eigenstate component $\langle\phi_1|$ is exactly expressed

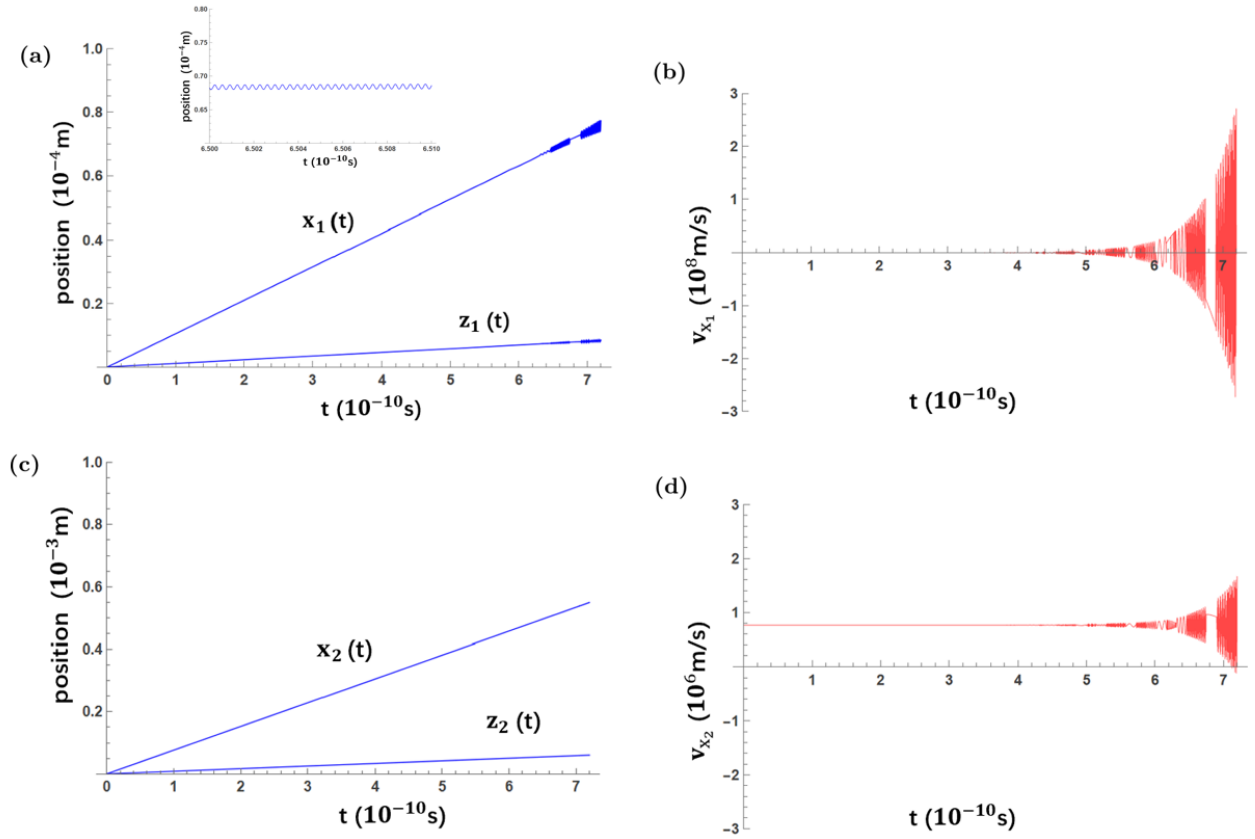


Figure 2: Time-dependent trajectory and velocity of holes governed by the non-Hermitian Luttinger Hamiltonian. (a) Time evolution of the heavy hole's position along x and z axes. The ZB effect is evident in the long-time limit. The inset reveals the microscopic ZB oscillations. (b) Time evolution of the heavy hole's velocity along x axis. The velocity is approximate to the speed of light in the long-time limit which is the disabled region. (c) Time evolution of the light hole's position along x and z axes. The positions are almost proportion to the time. (d) Time evolution of the light hole's velocity along x axis. The amplitude of velocity remains the order of 10^6 m/s.

as $\langle\phi_1| = \sqrt{\frac{k_x^2+k_y^2}{4k^2}}\big(-\frac{2k_z(-ik_x+k_y)}{(k_x-ik_y)^2}, -\frac{\sqrt{3}(k_x+ik_y)(\gamma_2+im\frac{\kappa}{k^2})}{(k_x-ik_y)\gamma_2}, 0, 1\big)$ and the right eigenstate $|\psi_1\rangle$ is expressed as $|\psi_1\rangle = \sqrt{\frac{k_x^2+k_y^2}{4k^2}}\big(-\frac{2k_z(ik_x+k_y)}{(k_x+ik_y)^2}, -\frac{\sqrt{3}(k_x-ik_y)(\gamma_2+im\frac{\kappa}{k^2})}{(k_x+ik_y)\gamma_2}, 0, 1\big)^T$. The dominate LH left eigenstate component $\langle\phi_2|$ is expressed as $\langle\phi_2| = \sqrt{\frac{k_x^2+k_y^2}{4k^2}}(\frac{\sqrt{3}(k_x+ik_y)(\gamma_2+im\frac{\kappa}{k^2})}{(k_x-ik_y)\gamma_2}, -\frac{2ik_z}{k_x-ik_y}, 1, 0)$ and the right eigenstate $|\psi_2\rangle$ is expressed as $|\psi_2\rangle = \sqrt{\frac{k_x^2+k_y^2}{4k^2}}(\frac{\sqrt{3}(k_x-ik_y)(\gamma_2+im\frac{\kappa}{k^2})}{(k_x+ik_y)\gamma_2}, \frac{2ik_z}{k_x+ik_y}, 1, 0)^T$.

Fig. 2 shows the position and velocity of a heavy hole and light hole over time. The trajectories and velocities for heavy and light holes along the x and y axes are indistinguishable. This is a direct consequence of the in-plane rotational isotropy of the spherical Luttinger Hamiltonian and our deliberately chosen symmetric initial conditions ($k_{x0} = k_{y0}$), which aim to simplify the problem and focus on the core non-Hermitian amplification mechanism. Therefore, to maintain conciseness, we restrict our primary discussion to the evolution along the x and z axes. A comprehensive collection of the three-dimensional trajectories and their respective velocity profiles is included in the Appendix B. As illustrated in Fig. 2(a), heavy hole's ZB effect becomes more and more evident

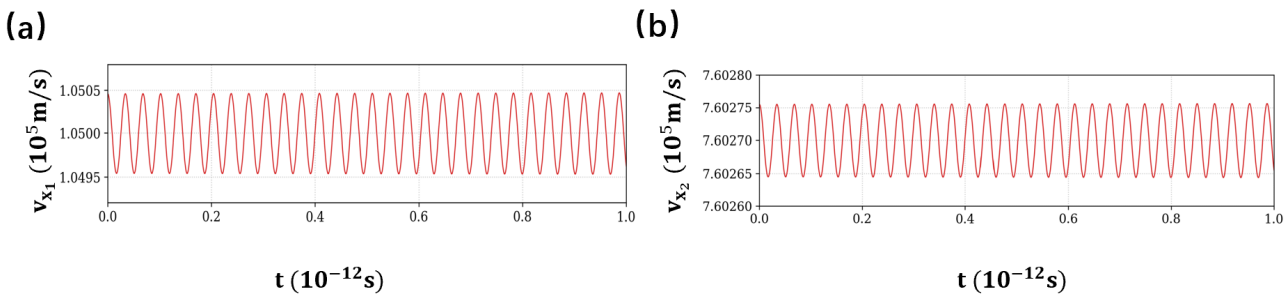


Figure 3: ZB velocity profiles within the realistic coherent window. (a) Heavy hole velocity $v_{x_1}(t)$ and (b) light hole velocity $v_{x_2}(t)$ up to 1.0 ps. Restricted to this physical timeframe which is prior to complete decoherence induced by continuous scattering, the non-Hermitian Luttinger model exhibits stable, non-divergent, and sinusoidal ZB oscillations, demonstrating the effective non-Hermitian amplification of the microscopic quantum interference.

as time evolves, at first glance, the macroscopic position-time trajectory appears as a straight line dominated by the semi-classical ballistic drift. This is due to the immense scale disparity: the macroscopic displacement is on the order of 10^{-4} m, which visually masks the spatial oscillations which is on the order of 10^{-6} m. However, as explicitly revealed in the highly magnified inset of Fig. 2(a), the particle exhibits oscillation which characterizes the ZB effect. We emphasize that the ZB effect intrinsically exists from the very beginning even at infinitesimally small t, rather than abruptly emerging only at late times. Because the spatial amplitude of ZB is inherently small on a macroscopic axis, the velocity profile Fig. 2(b) which is the time derivative of the position extracts the beat frequency ω as a magnifying prefactor, serves as the definitive observable for these non-Hermitian dynamics. The rapidly growing exponential envelope stretches the waveform vertically, creating a visual illusion of a shifted frequency in the time-domain linear plot. It is important to emphasize that the intrinsic interband beat frequency remains fundamentally unchanged within our first-order small-κ approximation. As dictated by the exact complex eigenvalues in Eq. (4), higher-order corrections will inevitably shift the real part of the beat frequency if the non-Hermitian coefficient increases beyond the perturbative regime. However, operating within the weak-dissipation limit, this higher-order frequency shift remains mathematically negligible, validating the utilization of the unperturbed interband frequency in our model (See Appendix D). In the long-time limit, the ZB velocity asymptotically approaches the speed of light. To comprehensively understand the system's underlying mechanism, we similarly examine the transient dynamics of a light-hole-dominated wave packet by setting $|c_1| \ll |c_2|$. Figs. 2(c) and 2(d) show the position and velocity of the light hole over time. Compared with the heavy hole, the light hole's oscillation amplitude is much smaller, and the oscillations are nearly imperceptible in the standard position plot. From Fig. 2(d), the light hole' s ZB effect is indeed not evident. Actually, this is just because the model failed in the long-time limit.

We next elucidate the underlying physical mechanism driving these distinct dynamic behaviors. Under continuous optical pumping, the system undergoes a distinctive two-stage evolution. Upon initial illumination, the system enters a transient non-equilibrium state. As introduced in our model, the pump laser drives electrons from the VBLH to the VBHH. Consequently, electron-electron scattering intensifies significantly in both the

upper and lower bands due to the highly excited non-equilibrium distribution. However, the continuous optical extraction from the VBLH and the subsequent accumulation in the VBHH creates a fundamental macroscopic asymmetry: the light holes acquire a robust net gain (a surplus of vacancies) while the heavy holes experience a pronounced net loss. As time progresses, this uncompensated collision asymmetry drives the non-Hermitian exponential gain. However, it is imperative to recognize that in semiconductor systems, this intensive inelastic scattering typically destroys phase coherence within a few picoseconds timescale. Therefore, to prevent the non-Hermitian amplification from entering unphysical divergences, we must restrict our analysis strictly to this initial picosecond regime, where the coherent ZB oscillations remain physically valid.

To maintain physical consistency, given that the oscillation velocity cannot exceed the speed of light (c), a temporal cutoff is required, estimated here at 7.2×10^{-10} s. It must be emphasized that the velocity approaching the speed of light is not a physical prediction of actual carrier transport, but rather a formal mathematical breakdown of the Luttinger model under unconstrained exponential gain. Therefore, we utilize c strictly as a relativistic causality boundary to determine this temporal cutoff. This cutoff defines the maximum validity window of our transient effective model. In realistic semiconductor systems, however, the physical validity window is significantly shorter than this mathematical cutoff. While carrier pumping and scattering provide the physical basis for the initial non-Hermitian amplification, the continuous accumulation of stochastic inelastic collisions is expected to destroy quantum phase coherence within a few picoseconds. Consequently, we evaluate the ZB dynamics only within this initial picosecond window, as explicitly detailed in the high-resolution transient velocity profiles of Fig. 3. It should be noted that all plotted positions and velocities in our figures represent the real parts of the normalized expectation values. As laboratory measurements exclusively yield real physical quantities, extracting the real part rigorously maps our complex non-Hermitian formalism onto macroscopically measurable signals, which will be detailed in the experimental scheme (Section 4). The corresponding imaginary part is associated with the non-Hermitian phase accumulation and does not contribute to the classical measured observables. This mathematical treatment accurately extracts the physically measurable kinematic observables from the complex non-Hermitian framework.

Specifically, Fig. 3(a) illustrates the heavy hole's velocity $v_{x_1}(t)$ oscillating around a macroscopic semiclassical drift of approximately 1.05×10^5 m/s. Within this physical 1.0-ps timeframe, the microscopic ZB interference amplitude experiences a steady non-Hermitian amplification while maintaining a coherent and stable sinusoidal waveform, entirely devoid of the unphysical divergence seen at macroscopic times. Similarly, Fig. 3(b) depicts the light hole's velocity $v_{x_2}(t)$, which centers around a notably higher drift velocity ($\sim 7.60\times10^5$ m/s) due to its smaller effective mass. Importantly, the light hole exhibits a weaker transient ZB amplitude, corroborating that the heavy hole's ZB effect is dynamically more dominant. These explicit picosecond-scale profiles demonstrate that our model effectively predicts the physically valid ZB enhancement right before complete decoherence occurs, successfully capturing the short-time ultrafast coherent dynamics long before the mathematical divergence at $\sim 10^{-10}$ s is ever reached. It is worth noting that accurately capturing the long-time dynamics and the eventual transition into a true non-equilibrium steady state would require a full open-system kinetic framework, which falls outside the scope of our current focus on short-time transient coherence.

To delineate the specific influence of non-hermiticity on the ZB effect, we benchmark our findings against the Hermitian limit by setting $\kappa = 0$. The dynamical velocity profiles for the heavy-hole-dominated wave

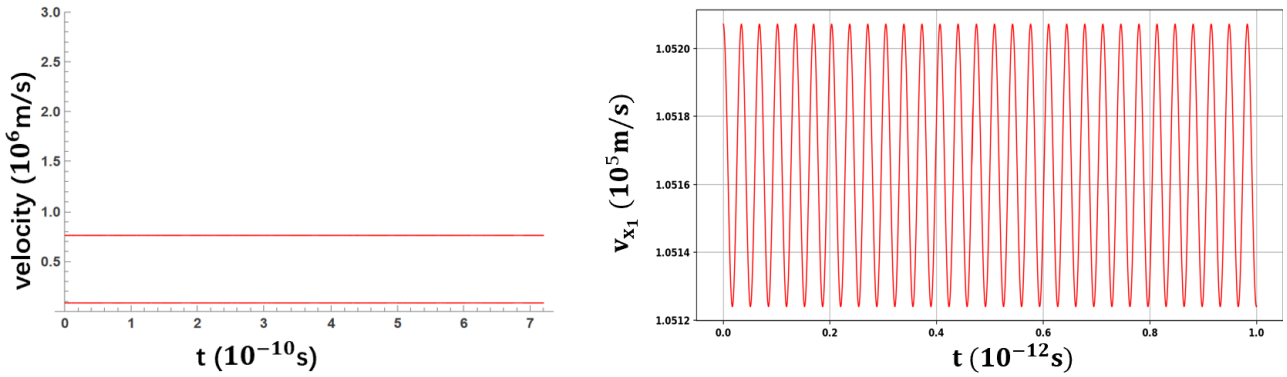


Figure 4: Time-dependent dynamics of the heavy hole in the Hermitian limit ($\kappa = 0$). (a) Macroscopic time evolution of the velocity (v_{x_1} and v_{z_1}) evaluated at a larger time scale (10^{-10} s), appearing as a constant macroscopic drift. (b) Microscopic time evolution of the velocity evaluated at the picosecond scale (10^{-12} s). In this unperturbed closed system, the intrinsic interband interference within the initial wave packet generates a baseline ZB oscillation. Crucially, this oscillation strictly maintains a constant amplitude without any exponential amplification.

packet within this standard Hermitian Luttinger framework are presented in Fig. 4, serving as a fundamental baseline for comparison (light hole's results are presented in Appendix B). On a macroscopic time scale (10^{-10} s) as shown in Fig. 4(a), the velocity appears featureless, presenting merely as a constant drift. However, in this unperturbed closed system, the intrinsic interband interference originating from the microscopic minority component of the initial wave packet inevitably triggers the ZB effect. As clearly revealed when zooming into the picosecond-scale profile (10^{-12} s) in Fig. 4(b), this baseline ZB manifests purely as a microscopic harmonic oscillation with a strictly constant amplitude. Because the energy spectrum in the Hermitian limit is entirely real, the evolution dynamics completely lack any exponential magnification mechanism.

3.2. Momentum-dependent dissipation model

We now turn to a more realistic scenario where the non-Hermitian parameter κ is no longer treated as a constant. Since the non-Hermiticity arises from scattering. The coupling strength should logically scale with the carrier velocity. We propose a phenomenological ansatz where κ is linearly proportional to the kinetic energy, reflecting the increased scattering probability at higher momenta. By setting $\kappa \propto \frac{k^2}{m}$, we define the effective non-Hermitian coupling as $\kappa = A\frac{k^2}{m}$, where A is a dimensionless scaling factor. This momentum-dependent dissipation introduces a self-consistent feedback between the carrier dynamics and the non-Hermitian amplification. Therefore, we have

$$\frac{\partial \hbar\omega}{\partial \mathbf{k}} = \frac{4\mathbf{k}\gamma_2}{m} + \frac{2iA\mathbf{k}}{m\gamma_2} - \frac{6iA\boldsymbol{k_z}\frac{\partial \boldsymbol{k_z}}{\partial \mathbf{k}}}{m\gamma_2}, \tag{13a}$$

$$\begin{aligned}\frac{\partial T}{\partial \mathbf{k}} =& (\frac{2\mathbf{k}\boldsymbol{\beta}}{k^4} - \frac{\boldsymbol{\beta}}{k^2})(1 - \frac{iA}{2\gamma_2}) - \frac{iA}{\gamma_2}[-(\frac{2\boldsymbol{k}\boldsymbol{\alpha}}{k^4} - \frac{\boldsymbol{\beta}}{k^2})\frac{3k_z^2}{2k^2} \\ &+ (\frac{3\boldsymbol{\alpha}}{2k^2} - \frac{15}{8}I_4)\frac{2k_z\frac{\partial \boldsymbol{k_z}}{\partial \mathbf{k}}k^2 - 2\mathbf{k}k_z^2}{k^4}],\end{aligned} \tag{13b}$$

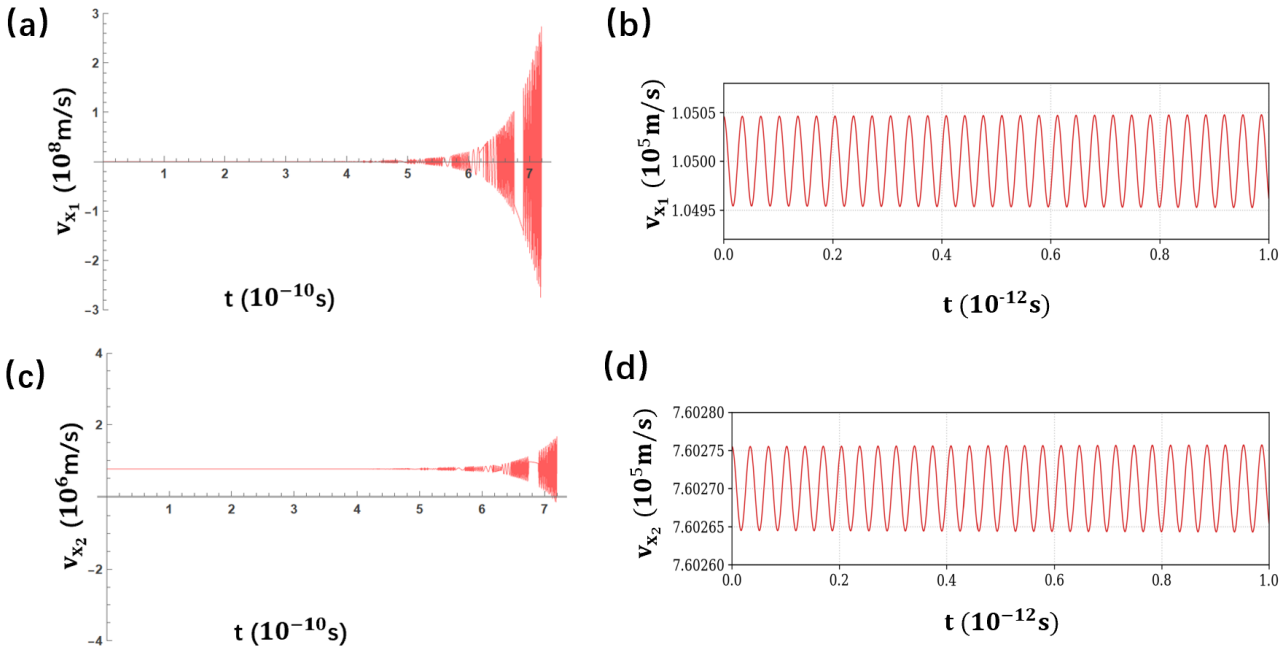


Figure 5: Time-dependent velocity of holes governed when κ is proportional to the kinetic energy. (a) Time evolution of the heavy hole's velocities along x axis, which asymptotically diverges toward the relativistic causality boundary. (b) Time evolution of the heavy hole's velocity along x axis within the 1-ps window. (c) Time evolution of the light hole's velocity along x axis over the long-time limit. (d) Time evolution of the light hole's velocity along x axis within the 1-ps window. Contrasting the macroscopic divergence in (a) and (c) with the highly stable sinusoidal oscillations in (b) and (d) explicitly demonstrates the model's validity in capturing the non-Hermitian amplified ZB effect prior to complete phase decoherence.

Substituting Eq. (13) into Eq. (9), holes' trajectory described by the Luttinger Hamiltonian is gotton. We take A's value as 6×10^{-3}. Applying the same initial conditions for the heavy and light holes, we explicitly contrast their long-time unconstrained mathematical velocity divergences with their short-time physical transient velocity profiles in Fig. 5. A comparison of Fig. 2 and Fig. 5 demonstrates that the holes' velocity oscillation patterns are robust against the specific form of κ. The trends remain qualitatively consistent with the constant-κ benchmark. This consistency is further corroborated by an order-of-magnitude analysis of Eqs. (12) and (13). The analysis reveals that the ZB oscillation amplitude maintains a consistent scale regardless of whether κ is constant or momentum-dependent. Since the non-Hermitian coefficient is sufficiently small to be treated as a perturbation, its functional dependence on momentum introduces only negligible corrections to the oscillation magnitude, resulting in the nearly identical trajectories observed in Figs. 2 and 5. To maintain mathematical consistency, if this momentum-dependent exponential gain were left unconstrained, the ZB velocity of the heavy holes would asymptotically approach the speed of light at $\tau \approx 7.2 \times 10^{-10}$ s. As emphasized previously, we utilize c strictly as a formal relativistic causality boundary marking the ultimate mathematical breakdown of the unconstrained Luttinger model. In a realistic semiconductor environment, however, continuous phase-breaking collisions will drive the system into a decoherent state within a much shorter timeframe. Consequently, Fig. 5 confirms that within the actual ultrafast coherent window, the momentum-dependent non-Hermitian model provides a stable,

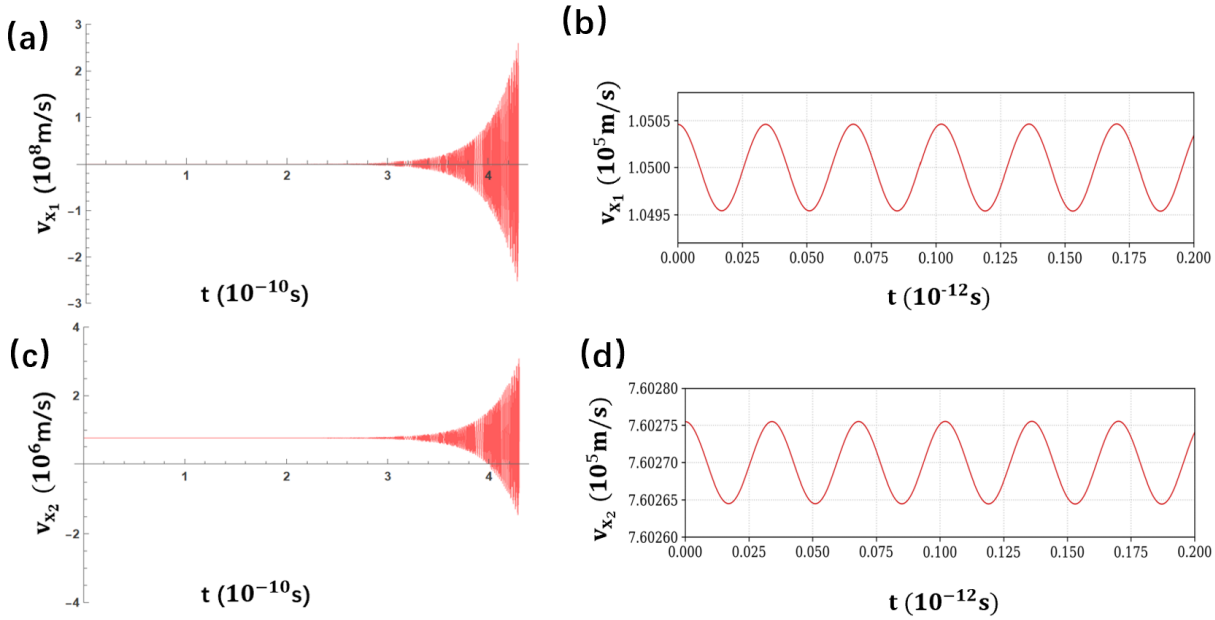


Figure 6: Time-dependent velocity of holes when $A = 10^{-2}$. (a) Heavy hole's velocity along x axis over long-time limit. (b) Heavy hole's velocity along x axis within coherent window. (c) Light hole's velocity along x axis over long-time limit. (d) Light hole's velocity along x axis within coherent window.

predictable, and physically valid representation of the amplified ZB effect right before complete decoherence occurs.

The influence of non-Hermiticity on ZB dynamics is further elucidated by scaling the factor to $A = 10^{-2}$. Mathematically, this increased dissipation accelerates the unconstrained exponential gain, which causes the causality-imposed temporal cutoff to contract from 7.2×10^{-10} s down to 4.3×10^{-10} s as depicted in figs. 6(a) and 6(c). This indicates that the strict validity window of our mathematical model becomes narrower. Physically, this larger non-Hermitian coefficient reflects an accelerated electronic redistribution driven by intensified electron-electron scattering. Consequently, the actual phase-coherence time of the system in reality should also be correspondingly shorter. However, despite this shortened physical coherent window, the stronger non-Hermitian term simultaneously magnifies the transient ZB interference amplitude. As explicitly demonstrated in the 0.2-ps velocity profiles (Fig. 6), the oscillation magnitude is enhanced right from the initial excitation. Taking both holes as quantitative examples within this 0.2-ps physical window: for the heavy hole, the maximum oscillation velocity was previously bounded at approximately 1.05046×10^5 m/s [Fig. 3(a)]. Under the enhanced coupling, this maximum velocity leaps to roughly 1.05077×10^5 m/s [Fig. 6(b)]. Similarly, for the light hole, the maximum velocity increases from approximately 7.60276×10^5 m/s [Fig. 3(b)] to roughly 7.60279×10^5 m/s [Fig. 6(d)]. This quantitative enhancement proves that a stronger non-Hermitian drive yields a larger transient ZB velocity signal before complete decoherence takes over. From an experimental perspective, the scattering intensity and thus the resulting effective non-Hermiticity can be tuned via thermal excitation. This approach provides a viable pathway to observe these transient ZB phenomena through temperature dependent transport measurements.

4. Experimental realization

Next, we propose a realizable experimental scheme utilizing ultrafast two-color pump-probe spectroscopy. A high-purity, intrinsic single-crystal Ge sample, characterized by an initial carrier concentration of less than 10^{12} cm^{-3}, is selected and cut along the [110] crystallographic orientation.

Because the valence band is entirely filled in intrinsic Ge at equilibrium, direct inter-valence-band transitions are initially forbidden by Pauli blocking. To overcome this, the preparation of the required hole population necessitates a multi-pulse optical excitation. First, an initial near-infrared (NIR) injection pulse, with a photon energy exceeding the fundamental bandgap, is applied [53]. Because our theoretical non-Hermitian term H_{loss} is band-selective but preserves spin degeneracy, this NIR injection utilizes linearly polarized light to produce a symmetric non-equilibrium population of holes. This choice preserves the spin degeneracy of H_{loss}, ensuring that the $+i\kappa$ and $-i\kappa$ structure is not broken by spin-dependent optical selection rules. Importantly, the NIR injection fluence is kept below a critical threshold to create sufficient initial vacancies in the VBHH to lift the Pauli blocking, while leaving the VBLH largely occupied to serve as an abundant electron source.

Shortly after this preparation (delayed to allow intraband thermalization but avoid recombination), a second, specifically tuned mid-infrared (MIR) or terahertz (THz) driving pulse is applied [54,55]. This pulse is resonantly tuned to the momentum-dependent HH–LH energy splitting. With the VBHH vacancies now available, the driving pulse successfully stimulates continuous inter-valence-band transitions [56]. The combination of the difference in density of states ($m_{HH} > m_{LH}$), the continuous optical extraction of electrons from the VBLH to the VBHH by the MIR/THz pump, and the intensified scattering rates collectively establishes the band-selective non-Hermitian gain/loss mechanism described in our model. Finally, a delayed non-perturbative probe pulse is utilized to detect the resulting ultrafast dynamics within the phase-coherence window. It is exactly at this detection stage that the theoretical biorthogonal quantities map onto the experimental observables. Specifically, the transient velocity of the carrier wavepacket, calculated theoretically via the real part of the normalized biorthogonal expectation value ($\mathrm{Re}[\langle\hat{v}(t)\rangle]$), maps directly onto the macroscopic differential transmission ($\Delta T/T$) or transient optical conductivity signals detected by this MIR/THz probe pulse.

5. Conclusion

In this work, we have established a universal theoretical framework for the Zitterbewegung effect in non-Hermitian systems. Our analysis demonstrates that while non-Hermiticity preserves the structural form of the ZB equations, it introduces an exponential growth factor that fundamentally amplifies the trembling motion beyond Hermitian limits. By implementing this framework within the Luttinger Hamiltonian, we demonstrate that the non-Hermitian coefficient κ, which phenomenologically represents the intensified carrier collisions driven by continuous optical pumping, acts as an amplifier for the intrinsic ZB effect. Our analysis reveals that within the weak-dissipation limit (the first-order small-κ approximation), the fundamental ZB beat frequency remains securely tied to the unperturbed interband energy gaps, the non-Hermiticity introduces an exponential growth in the oscillation magnitude.

Crucially, our theoretical framework specifically targets the ultrafast transient regime rather than long-term steady states. We emphasize that this amplified trembling motion should be captured within a sub-picosecond

to picosecond window, bounded fundamentally by the carrier phase-coherence time, before the linear non-Hermitian approximation naturally breaks down. To physicalize this theoretical model, we propose a feasible time-resolved two-color pump-probe spectroscopy scheme in intrinsic germanium. By carefully controlling the NIR injection fluence and utilizing linearly polarized light, this experimental design successfully overcomes Pauli-blocking limitations while preserving the spin-degenerate mathematical structure of our effective non-Hermitian operator.

Ultimately, this work fundamentally bridges the gap between the theoretical physics of open quantum systems and realistic ultrafast semiconductor spectroscopy, offering a robust and rigorous paradigm to explore quantum coherence and complex carrier transport.

Appendix A: Derivation of the projection operators

In this section, we provide a detailed derivation of the projection operators for the non-Hermitian Luttinger Hamiltonian. Ignoring the normalization coefficient, the right vectors of the Hamiltonian are

$$\begin{aligned}
|\psi_1\rangle &= (-\frac{2k_z(ik_x+ik_y)}{(k_x+ik_y)^2}, -\frac{(k^2-3k_z^2)\gamma_2+2im\kappa+2\sqrt{k^4\gamma_2^2+im(k^2-3k_z^2)\gamma_2\kappa-m^2\kappa^2}}{\sqrt{3}(k_x+ik_y)^2\gamma_2}, 0, 1),\\
|\psi_2\rangle &= (\frac{(k^2-3k_z^2)+2im\kappa-2\sqrt{k^4\gamma_2^2+im(k^2-3k_z^2)\gamma_2\kappa-m^2\kappa^2}}{\sqrt{3}(k_x+ik_y)^2\gamma_2}, \frac{2ik_z}{k_x+ik_y}, 1, 0),\\
|\psi_3\rangle &= (-\frac{2k_z(ik_x+ik_y)}{(k_x+ik_y)^2}, -\frac{(k^2-3k_z^2)+2im\kappa-2\sqrt{k^4\gamma_2^2+im(k^2-3k_z^2)\gamma_2\kappa-m^2\kappa^2}}{\sqrt{3}(k_x+ik_y)^2\gamma_2}, 0, 1),\\
|\psi_4\rangle &= (\frac{(k^2-3k_z^2)\gamma_2+2im\kappa+2\sqrt{k^4\gamma_2^2+im(k^2-3k_z^2)\gamma_2\kappa-m^2\kappa^2}}{\sqrt{3}(k_x+ik_y)^2\gamma_2}, \frac{2ik_z}{k_x+ik_y}, 1, 0),
\end{aligned} \tag{14}$$

with corresponding energies

$$\epsilon_{3,4(1,2)} = \frac{k^2\gamma_1 \pm 2\sqrt{k^4\gamma_2^2+im(k^2-3k_z^2)\gamma_2\kappa-m^2\kappa^2}}{2m}. \tag{15}$$

Here, $|\psi_1\rangle$ and $|\psi_2\rangle$ represent the heavy hole states while $|\psi_3\rangle$ and $|\psi_4\rangle$ are identified as the light hole states. We introduce the approximation $m^2\kappa^2 \ll k^4\gamma_2^2$ and expand states and energies to the first Taylor series, then the approximation is

$$\begin{aligned}
|\psi_1\rangle &= \frac{1}{A}(-\frac{2k_z(ik_x+ik_y)}{(k_x+ik_y)^2}, -\frac{\sqrt{3}(k_x-ik_y)(\gamma_2+im\frac{\kappa}{k^2})}{(k_x+ik_y)\gamma_2}, 0, 1),\\
|\psi_2\rangle &= \frac{1}{B}(\frac{(k^2+3k_z^2)(-\gamma_2+\frac{im\kappa}{k^2})}{\sqrt{3}(k_x+ik_y)^2\gamma_2}, \frac{2ik_z}{k_x+ik_y}, 1, 0),\\
|\psi_3\rangle &= \frac{1}{B}(-\frac{2k_z(ik_x+k_y)}{(k_x+ik_y)^2}, -\frac{(k^2+3k_z^2)(-\gamma_2+\frac{im\kappa}{k^2})}{\sqrt{3}(k_x+ik_y)^2\gamma_2}, 0, 1),\\
|\psi_4\rangle &= \frac{1}{A}(\frac{\sqrt{3}(k_x-ik_y)(\gamma_2+im\frac{\kappa}{k^2})}{(k_x+ik_y)\gamma_2}, \frac{2ik_z}{k_x+ik_y}, 1, 0),
\end{aligned} \tag{16}$$

with corresponding energies

$$\epsilon_{3,4(1,2)} = \frac{k^2\gamma_1 \pm 2k^2\gamma_2 \pm \frac{im\kappa(k^2-3k_z^2)}{k^2\gamma_2}}{2m}, \tag{17}$$

Where normalized coefficients are defined as:

$$\begin{aligned} A &= (\frac{4k^2}{k_x^2+k_y^2})^{\frac{1}{2}}, \\ B &= (\frac{4k^2(k^2+3k_z^2)}{3(k_x^2+k_y^2)^2})^{\frac{1}{2}}. \end{aligned} \tag{18}$$

Similarly, the left vectors of the Hamiltonian are derived as:

$$\begin{aligned} \langle\phi_1| &= \frac{1}{A}(-\frac{2k_z(-ik_x+k_y)}{(k_x-ik_y)^2}, -\frac{\sqrt{3}(k_x+ik_y)(\gamma_2+im\frac{\kappa}{k^2})}{(k_x-ik_y)\gamma_2}, 0, 1)^T, \\ \langle\phi_2| &= \frac{1}{B}(\frac{(k^2+3k_z^2)(-\gamma_2+im\frac{\kappa}{k^2})}{\sqrt{3}(k_x-ik_y)^2\gamma_2}, \frac{-2ik_z}{k_x-ik_y}, 1, 0)^T, \\ \langle\phi_3| &= \frac{1}{B}(-\frac{2k_z(-ik_x+k_y)}{(k_x-ik_y)^2}, -\frac{(k^2+3k_z^2)(-\gamma_2+im\frac{\kappa}{k^2})}{\sqrt{3}(k_x-ik_y)^2\gamma_2}, 0, 1)^T, \\ \langle\phi_4| &= \frac{1}{A}(\frac{\sqrt{3}(k_x+ik_y)(\gamma_2+im\frac{\kappa}{k^2})}{(k_x-ik_y)\gamma_2}, \frac{-2ik_z}{k_x-ik_y}, 1, 0)^T. \end{aligned} \tag{19}$$

In non-Hermitian systems, the projection operator for the j-th subspace is defined using the biorthogonal basis: $Q_j = \sum |\psi_j\rangle\langle u_j|$. The finalized left eigenvectors $\langle u_i|$ must satisfy the strict biorthonormality condition $\langle u_i|\psi_j\rangle = \delta_{ij}$. First, we obtain the raw left eigenvectors, denoted as $|\phi_i\rangle$, which satisfy the adjoint eigenvalue equation $H^\dagger|\phi_i\rangle = \epsilon_i^*|\phi_i\rangle$. However, due to the inherent twofold degeneracy within the heavy and light hole bands, these raw left eigenvectors are not automatically orthogonal to the right eigenvectors of the other degenerate state within the same subspace (i.e., $\langle\phi_1|\psi_2\rangle \neq 0$). To rigorously resolve this degeneracy and construct a valid biorthogonal basis, we implement a generalized Gram-Schmidt biorthogonalization procedure for the degenerate pairs. By subtracting the non-orthogonal projections, the properly orthogonalized left eigenvectors $|u_1\rangle$ and $|u_2\rangle$ are constructed as:

$$\begin{aligned} H^\dagger|u_1\rangle &= \epsilon^*|u_1\rangle, \\ H^\dagger|u_2\rangle &= \epsilon^*|u_2\rangle, \\ |u_1\rangle &= |\phi_2\rangle - \frac{\langle\psi_1|\phi_2\rangle}{\langle\psi_1|\phi_1\rangle}|\phi_1\rangle, \\ |u_2\rangle &= |\phi_1\rangle - \frac{\langle\psi_2|\phi_1\rangle}{\langle\psi_2|\phi_2\rangle}|\phi_2\rangle. \end{aligned} \tag{20}$$

Based on this explicit construction, we have rigorously verified via symbolic computation that these operators satisfy the required projection algebra up to the first-order approximation: $Q_L^2 = Q_L$, $Q_H^2 = Q_H$, $Q_L Q_H = 0$, and the completeness relation $Q_L + Q_H = I_4$.

For further computational convenience, we introduce the asymptotic approximation $k_z \ll k_y$, k_x and adopt the specific scaling relation $k_z \approx \frac{1}{10}k_x = \frac{1}{10}k_y$. Under this approximation, the explicit forms of the orthogonal left eigenvectors are obtained as:

$$\begin{aligned} \langle u_1| = &\frac{k^2+3k_z^2}{2k\sqrt{k_x^2+k_y^2}}(1-\frac{3(k_x^2+k_y^2)}{2k^2}\frac{im\kappa}{k^2\gamma_2}) \\ &\Big(\frac{2k_z(k_y+ik_x)}{(k_x+ik_y)^2}\frac{m^2\kappa^2}{k^4\gamma_2^2}, -\frac{\sqrt{3}(k_x+ik_y)^2}{k^2+3k_z^2}(1+\frac{im\kappa}{k^2\gamma_2}), -\frac{2\sqrt{3}k_z(k_y-ik_x)}{k^2+3k_z^2}(1+\frac{im\kappa}{k^2\gamma_2}), 1\Big)^T, \end{aligned}$$

$$
\begin{aligned}
\langle u_2| &= \frac{\sqrt{3(k^2+3k_z^2)}}{2k}(1+\frac{k^2+3k_z^2}{2k^2}\frac{im\kappa}{k^2\gamma_2}) \\
&\Big(\frac{k_x+ik_y}{\sqrt{3}(k_x-ik_y)}(-1+\frac{im\kappa}{k^2\gamma_2}), -\frac{2ik_z}{k_x+ik_y}\frac{m^2\kappa^2}{k^4\gamma_2^2}, 1, -\frac{2k_z}{\sqrt{3}(k_x-ik_y)}(1-\frac{im\kappa}{k^2\gamma_2})\Big)^T, \\
\langle u_3| &= \frac{\sqrt{3(k^2+3k_z^2)}}{2k}(1+\frac{k^2+3k_z^2}{2k^2}\frac{im\kappa}{k^2\gamma_2}) \\
&\Big(\frac{2k_z(k_y+ik_x)}{(k_x+ik_y)^2}\frac{m^2\kappa^2}{k^4\gamma_2^2}, \frac{k_x+ik_y}{\sqrt{3}(k_x-ik_y)}(1-\frac{im\kappa}{k^2\gamma_2}), \frac{2k_z}{\sqrt{3}(k_y+ik_x)}(1-\frac{im\kappa}{k^2\gamma_2}), 1\Big)^T, \\
\langle u_4| &= \frac{k^2+3k_z^2}{2k\sqrt{k_x^2+k_y^2}}(1-\frac{3(k_x^2+k_y^2)}{2k^2}\frac{im\kappa}{k^2\gamma_2}) \\
&\Big(\frac{\sqrt{3}(k_x+ik_y)^2}{k^2+3k_z^2}(1+\frac{im\kappa}{k^2\gamma_2}), -\frac{2ik_z}{k_x+ik_y}\frac{m^2\kappa^2}{k^4\gamma_2^2}, 1, \frac{2\sqrt{3}k_z(k_y+ik_x)}{k^2+3k_z^2}(1+\frac{im\kappa}{k^2\gamma_2})\Big)^T.
\end{aligned} \tag{21}
$$

By invoking the approximation $m^2\kappa^2 \ll k^4\gamma_2^2$, the higher order term can be neglected ($\frac{m^2\kappa^2}{k^4\gamma_2^2} \approx 0$), which simplifies the orthogonal left eigenvectors to:

$$
\begin{aligned}
\langle u_1| &= \frac{k^2+3k_z^2}{2k\sqrt{k_x^2+k_y^2}}(1-\frac{3(k_x^2+k_y^2)}{2k^2}\frac{im\kappa}{k^2\gamma_2})(0, -\frac{\sqrt{3}(k_x+ik_y)^2}{k^2+3k_z^2}(1+\frac{im\kappa}{k^2\gamma_2}), -\frac{2\sqrt{3}k_z(k_y-ik_x)}{k^2+3k_z^2}(1+\frac{im\kappa}{k^2\gamma_2}), 1)^T, \\
\langle u_2| &= \frac{\sqrt{3(k^2+3k_z^2)}}{2k}(1+\frac{k^2+3k_z^2}{2k^2}\frac{im\kappa}{k^2\gamma_2})(\frac{k_x+ik_y}{\sqrt{3}(k_x-ik_y)}(-1+\frac{im\kappa}{k^2\gamma_2}), 0, 1, -\frac{2k_z}{\sqrt{3}(k_x-ik_y)}(1-\frac{im\kappa}{k^2\gamma_2}))^T, \\
\langle u_3| &= \frac{\sqrt{3(k^2+3k_z^2)}}{2k}(1+\frac{k^2+3k_z^2}{2k^2}\frac{im\kappa}{k^2\gamma_2})(0, \frac{k_x+ik_y}{\sqrt{3}(k_x-ik_y)}(1-\frac{im\kappa}{k^2\gamma_2}), \frac{2k_z}{\sqrt{3}(k_y+ik_x)}(1-\frac{im\kappa}{k^2\gamma_2}), 1)^T, \\
\langle u_4| &= \frac{k^2+3k_z^2}{2k\sqrt{k_x^2+k_y^2}}(1-\frac{3(k_x^2+k_y^2)}{2k^2}\frac{im\kappa}{k^2\gamma_2})(\frac{\sqrt{3}(k_x+ik_y)^2}{k^2+3k_z^2}(1+\frac{im\kappa}{k^2\gamma_2}), 0, 1, \frac{2\sqrt{3}k_z(k_y+ik_x)}{k^2+3k_z^2}(1+\frac{im\kappa}{k^2\gamma_2}))^T.
\end{aligned} \tag{22}
$$

Combining the approximate right eigenvectors in Eq. (16) and the simplified orthogonal left eigenvectors in Eq. (22), we calculate the outer product of the eigenstates as follows:

$$
|\psi_1\rangle\langle u_1| = \begin{pmatrix}
0 & \frac{\sqrt{3}k_z(ik_x+k_y)}{2k^2}E & \frac{\sqrt{3}k_z^2(k_x^2+k_y^2)}{k^2(k_x+ik_y)^2}E & -\frac{k_z(ik_x+k_y)(k^2+3k_z^2)}{2k^2(k_x+ik_y)^2}F \\
0 & \frac{3k^2-3k_z^2}{4k^2}G & -\frac{3k_z(ik_x+k_y)}{2k^2}G & -\frac{\sqrt{3}(k^2+3k_z^2)(k_x^2+k_y^2)}{4k^2(k_x+ik_y)^2}E \\
0 & 0 & 0 & 0 \\
0 & -\frac{\sqrt{3}(k_x+ik_y)^2}{4k^2}E & -\frac{\sqrt{3}k_z(k_y-ik_x)}{2k^2}E & \frac{k^2+3k_z^2}{4k^2}F
\end{pmatrix}, \tag{23}
$$

$$
|\psi_2\rangle\langle u_2| = \begin{pmatrix}
\frac{k^2+3k_z^2}{4k^2}F & 0 & -\frac{\sqrt{3}(k^2+3k_z^2)(k_x^2+k_y^2)}{4k^2(k_x+ik_y)^2}E & \frac{k_z(ik_x+k_y)(k^2+3k_z^2)}{2k^2(k_x+ik_y)^2}F \\
\frac{\sqrt{3}k_z(k_y-ik_x)}{2k^2}E & 0 & \frac{3(k_y+ik_x)k_z}{2k^2}G & \frac{\sqrt{3}k_z^2(k_x^2+k_y^2)}{k^2(k_x+ik_y)^2}E \\
-\frac{\sqrt{3}(k_x+ik_y)^2}{4k^2}E & 0 & \frac{3k^2-3k_z^2}{4k^2}G & -\frac{\sqrt{3}k_z(ik_x+k_y)}{2k^2}E \\
0 & 0 & 0 & 0
\end{pmatrix}, \tag{24}
$$

$$
|\psi_3\rangle\langle u_3| = \begin{pmatrix}
0 & -\frac{\sqrt{3}k_z(ik_x+k_y)}{2k^2}E & -\frac{\sqrt{3}k_z^2(k_x^2+k_y^2)}{k^2(k_x+ik_y)^2}E & -\frac{3k_z(ik_x+k_y)(k_x^2+k_y^2)}{2k^2(k_x+ik_y)^2}G \\
0 & \frac{k^2+3k_z^2}{4k^2}F & \frac{k_z(k^2+3k_z^2)}{2k^2(ik_x-k_y)}F & \frac{\sqrt{3}(k_x^2+k_y^2)(k^2+3k_z^2)}{4k^2(k_x+ik_y)^2}E \\
0 & 0 & 0 & 0 \\
0 & \frac{\sqrt{3}(k_x+ik_y)^2}{4k^2}E & \frac{\sqrt{3}k_z(k_y-ik_x)}{2k^2}E & \frac{3k^2-3k_z^2}{4k^2}G
\end{pmatrix}, \tag{25}
$$

$$|\psi_4\rangle\langle u_4| = \begin{pmatrix} \frac{3k^2-3k_z^2}{4k^2}G & 0 & \frac{\sqrt{3}(k^2+3k_z^2)(k_X^2+k_y^2)}{4k^2(k_x+ik_y)^2}E & \frac{3k_z(k_y+ik_x)(k_x^2+k_y^2)}{2k^2(k_x+ik_y)^2}G \\ \frac{\sqrt{3}k_z(ik_x-k_y)}{2k^2}E & 0 & \frac{k_z(k^2+3k_z^2)}{2(k_y-ik_x)k^2}F & -\frac{\sqrt{3}k_z^2(k_x^2+k_y^2)}{k^2(k_x+ik_y)^2}E \\ \frac{\sqrt{3}(k_x+ik_y)^2}{4k^2}E & 0 & \frac{k^2+3k_z^2}{4k^2}F & \frac{\sqrt{3}k_z(k_y+ik_x)}{2k^2}E \\ 0 & 0 & 0 & 0 \end{pmatrix}, \tag{26}$$

where complex factors $E = 1 - \frac{im\kappa}{2k^2\gamma_2} + \frac{3k_z^2}{2k^2}\frac{im\kappa}{k^2\gamma_2}$, $F = 1 - \frac{3im\kappa}{2k^2\gamma_2} + \frac{3k_z^2}{2k^2}\frac{im\kappa}{k^2\gamma_2}$, $G = 1 + \frac{im\kappa}{2k^2\gamma_2} + \frac{3k_z^2}{2k^2}\frac{im\kappa}{k^2\gamma_2}$. Based on the above outer product results, we further construct the total projection operators for the light hole and heavy hole subspaces respectively. The projection operator for the heavy hole subspace Q_H and the light hole subspace Q_L are given by the sum of the corresponding single-state projection operators:

$$\begin{aligned} Q_H &= |\psi_1\rangle\langle u_1| + |\psi_2\rangle\langle u_2| = (\frac{(\mathbf{k}\cdot\mathbf{S})^2}{2k^2} - \frac{1}{8})E - \frac{3k_z^2}{4k^2}\frac{im\kappa}{k^2\gamma_2}I_4 - \frac{4S_z^4 + S_z^2 - 17I_4}{22}\frac{im\kappa}{k^2\gamma_2}, \\ Q_L &= |\psi_3\rangle\langle u_3| + |\psi_4\rangle\langle u_4| = I_4 - (\frac{(\mathbf{k}\cdot\mathbf{S})^2}{2k^2} - \frac{1}{8})E + \frac{3k_z^2}{4k^2}\frac{im\kappa}{k^2\gamma_2}I_4 + \frac{4S_z^4 + S_z^2 - 17I_4}{22}\frac{im\kappa}{k^2\gamma_2}, \end{aligned} \tag{27}$$

where I_4 is the 4-dimensional identity matrix and the spin matrices S_x,S_y and S_z are defined as:

$$\begin{aligned} S_x &= \begin{pmatrix} 0 & i\frac{\sqrt{3}}{2} & 0 & 0 \\ -i\frac{\sqrt{3}}{2} & 0 & i & 0 \\ 0 & -i & 0 & i\frac{\sqrt{3}}{2} \\ 0 & 0 & -i\frac{\sqrt{3}}{2} & 0 \end{pmatrix}, \\ S_y &= \begin{pmatrix} 0 & \frac{\sqrt{3}}{2} & 0 & 0 \\ \frac{\sqrt{3}}{2} & 0 & 1 & 0 \\ 0 & 1 & 0 & \frac{\sqrt{3}}{2} \\ 0 & 0 & \frac{\sqrt{3}}{2} & 0 \end{pmatrix}, \\ S_z &= \begin{pmatrix} \frac{3}{2} & 0 & 0 & 0 \\ 0 & \frac{1}{2} & 0 & 0 \\ 0 & 0 & -\frac{1}{2} & 0 \\ 0 & 0 & 0 & -\frac{3}{2} \end{pmatrix}. \end{aligned} \tag{28}$$

Appendix B: The Zitterbewegung effect in some cases

In this section, we systematically investigate the time-dependent Zitterbewegung dynamics of heavy and light holes in the non-Hermitian regime, including their spatial trajectories and velocity evolutions along the x, y and z axes. We also present a direct comparison with the Hermitian case to highlight the non-Hermitian effects on the Zitterbewegung motion.

All the time-resolved spatial trajectories and velocity profiles of heavy holes and light holes in the non-Hermitian regime with a constant non-Hermitian parameter κ are presented in Fig. 7. Figs. 7(a)-(c) depict the time-dependent translational motion of heavy holes along the x, y and z axes respectively, which show the oscillatory ZB behavior in non-Hermitian case. It is evident that the trajectories along the x and y axes are almost indistinguishable. Figs. 7(d)-(f) display the corresponding velocity evolutions of heavy holes along the

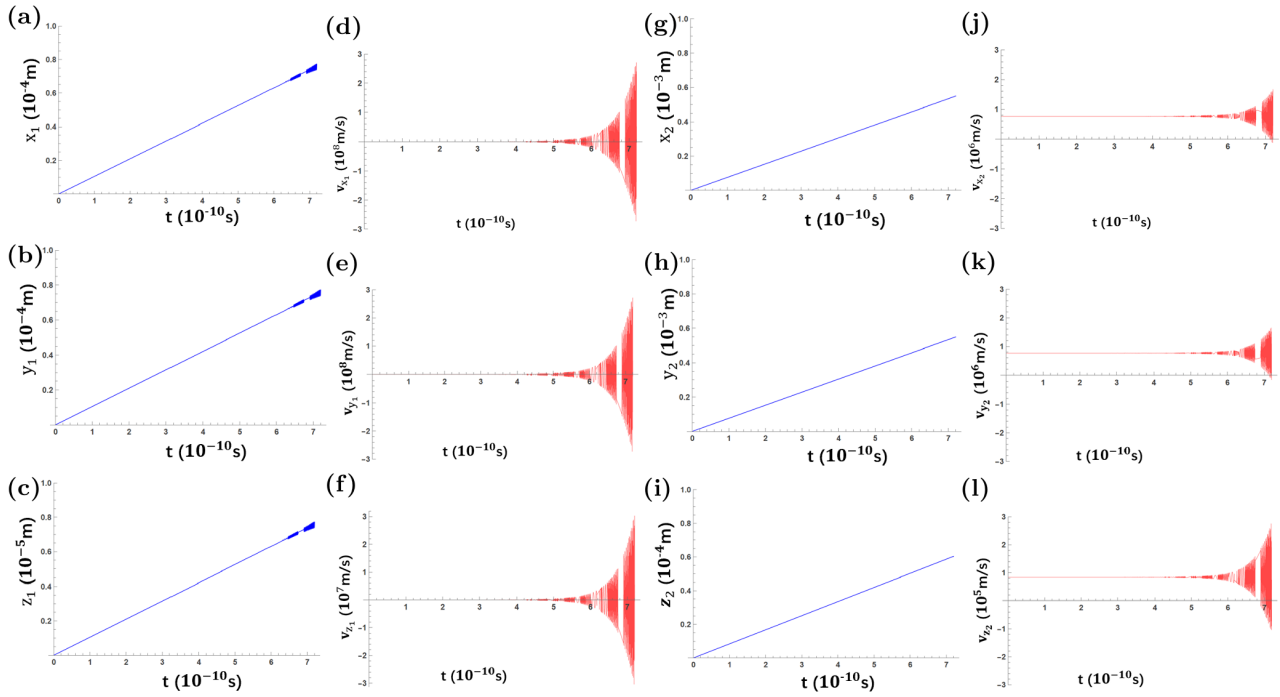


Figure 7: Time-dependent trajectory and velocity of holes when κ is a constant. (a)-(c) Heavy hole's motion along x,y,z axes. (d)-(f) Heavy hole's velocity along x,y,z axes. (g)-(i) Light hole's motion along x,y,z axes. (j)-(l) Light hole's velocity along x,y,z axes.

three axes, where the velocity oscillations are found to be correlated with the spatial ZB and exhibit amplitude modification induced by non-Hermiticity. For light holes, their spatial Zitterbewegung trajectories along the x, y and z axes are shown in Figs 7(g)-(i), and the associated velocity oscillations are illustrated in Figs. 7(j)-(l). It is evident that the non-Hermitian term leads to a noticeable change in the oscillation amplitude and phase of both the spatial trajectory and velocity of light holes, which is a key signature of non-Hermitian Zitterbewegung.

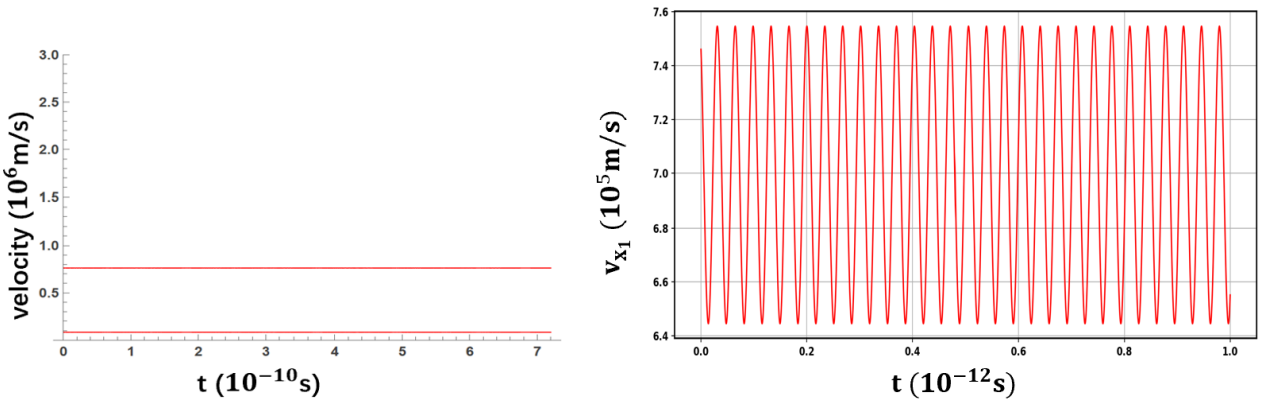


Figure 8: Time-dependent dynamics of the light hole in the Hermitian limit. (a) Macroscopic time evolution of the light hole's velocity. (b) Microscopic time evolution of the velocity v_{x1} evaluated at the picosecond scale (10^{-12} s).

Velocities along the x and z axes at a larger time scale ($10^{-10}s$) and the velocity along the x axis at the picosecond scale of the light hole in Hermitian case are presented in Fig. 8.

Appendix C: Perturbative mapping of the band-dependent non-Hermitian term

To demonstrate how the fixed spin-basis non-Hermitian operator acts as a band-selective dissipation mechanism in the momentum space, we employ first-order non-Hermitian perturbation theory.

First, we express the phenomenological non-Hermitian matrix $H_{loss} = \mathrm{diag}(i\kappa, -i\kappa, -i\kappa, i\kappa)$ using the fundamental angular momentum operator S_z for spin-3/2 systems. Squaring the S_z operator yields diagonal elements $(9/4, 1/4, 1/4, 9/4)$. Thus, H_{loss} can be written as:

$$H_{loss} = i\kappa \left(S_z^2 - \frac{5}{4} I_4 \right) \tag{29}$$

where I_4 is the 4×4 identity matrix. This expression confirms that the external optical pumping couples to the squared projection of the angular momentum along the laboratory z-axis.

Next, we consider the unperturbed Hermitian Luttinger Hamiltonian $H_0(\mathbf{k})$. Let $V(\mathbf{k})$ be the unitary transformation matrix that diagonalizes $H_0(\mathbf{k})$, and let $|\Psi_n(\mathbf{k})\rangle$ be its eigenstates. The total Hamiltonian is $H(\mathbf{k}) = H_0(\mathbf{k}) + H_{loss}$.

By transforming H_{loss} into the local energy eigenbasis, we obtain the effective non-Hermitian scattering matrix $\tilde{H}_{loss}(\mathbf{k})$:

$$\tilde{H}_{loss}(\mathbf{k}) = V^\dagger(\mathbf{k}) H_{loss} V(\mathbf{k}) \tag{30}$$

In our investigated parameter regime, the non-Hermitian coefficient κ acts as a small perturbation compared to the energy gap of the VBHH and VBLH ($\kappa \ll |E_{HH} - E_{LH}|$). Under this perturbative limit, the first-order complex energy correction ΔE_n for the n-th band is determined by the diagonal expectation values of $\tilde{H}_{loss}(\mathbf{k})$:

$$\begin{aligned} \Delta E_n(\mathbf{k}) &= \langle \Psi_n(\mathbf{k}) | H_{loss} | \Psi_n(\mathbf{k}) \rangle \\ &= i\kappa \left(\langle \Psi_n(\mathbf{k}) | S_z^2 | \Psi_n(\mathbf{k}) \rangle - \frac{5}{4} \right) \end{aligned} \tag{31}$$

Within our specific active momentum window ($k_x \approx k_y \gg k_z$), the carrier momentum lies predominantly in the $x-y$ plane. It is crucial to note that the true eigenstates $|\Psi_n(\mathbf{k})\rangle$ of the Luttinger Hamiltonian in this regime are helicity eigenstates, which are quantized along the momentum direction, rather than being pure states in the fixed laboratory S_z basis. Consequently, evaluating the expectation value $\langle S_z^2 \rangle$ requires projecting these helicity states onto the fixed z-axis.

Assuming the local momentum is aligned along the x-axis without loss of generality, the helicity eigenstate satisfies $S_x|\Psi_n\rangle = m_h|\Psi_n\rangle$, meaning we have $\langle S_x^2 \rangle = m_h^2$ exactly. Because the momentum lies in the $x-y$ plane, the laboratory z-axis is perpendicular to the helicity axis. The rotational symmetry about the helicity axis then gives $\langle S_y^2 \rangle = \langle S_z^2 \rangle$. By utilizing the relation $S^2 = S_x^2 + S_y^2 + S_z^2 = S_x^2 + 2S_z^2$, we can determine the z-axis projection. For the heavy hole states, the helicity is $m_h = \pm 3/2$. The projection yields $\langle S_z^2 \rangle_{HH} = (15/4 - 9/4)/2 = 3/4$. Similarly, for the light hole states with helicity $m_h = \pm 1/2$, the projection yields $\langle S_z^2 \rangle_{LH} = (15/4 - 1/4)/2 = 7/4$.

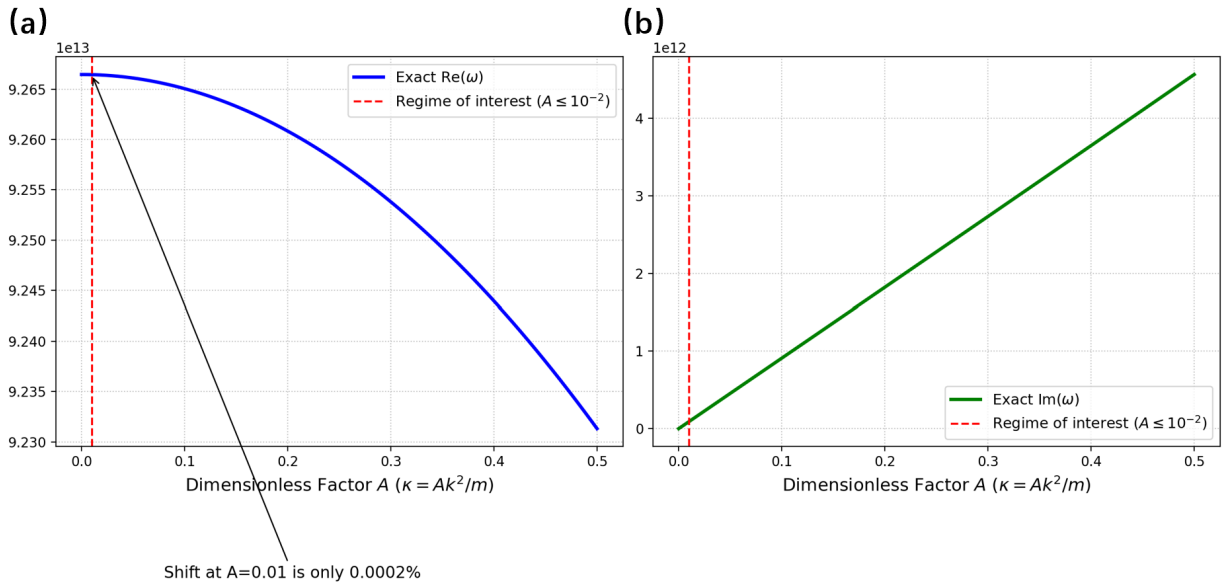


Figure 9: Numerical analysis of the ZB beat frequency ω versus the non-Hermitian coupling parameter A. (a) The real part $\mathrm{Re}(\omega)$ remains extremely stable within the weak-dissipation perturbative regime. At the maximum utilized parameter $A = 10^{-2}$ (red dashed line), the relative shift in the macroscopic oscillation frequency is mathematically negligible (less than 0.001%). (b) The imaginary part $\mathrm{Im}(\omega)$ exhibits a linear dependence on A, driving the accelerated exponential amplification of the transient ZB amplitude.

Substituting these exact expectation values into Eq. (31), we obtain the effective complex energy corrections:

$$\begin{aligned} \Delta E_{HH} &= i\kappa \left(\frac{3}{4} - \frac{5}{4} \right) = -i\frac{\kappa}{2}, \\ \Delta E_{LH} &= i\kappa \left(\frac{7}{4} - \frac{5}{4} \right) = +i\frac{\kappa}{2}. \end{aligned} \tag{32}$$

This rigorous perturbative mapping explicitly resolves the apparent basis discrepancy. It proves that the S_z^2-dependent operator, while defined in the fixed spatial frame, perfectly manifests as a band-dependent non-Hermitian mechanism in the momentum space: the VBHH uniquely acquires a negative imaginary correction (effective loss), while the VBLH uniquely acquires a positive imaginary correction (effective gain).

Appendix D: Exact numerical analysis of the beat frequency

To clarify the regime of validity for the constant frequency approximation utilized in our non-Hermitian Luttinger model, we evaluate the exact complex eigenvalues without the first-order Taylor expansion. As dictated by Eq. (4), the exact energy difference ΔE inherently contains a higher-order κ^2 correction term under the square root.

By modeling non-Hermitian coefficient as $\kappa = Ak^2/m$, we numerically compute both the real part and the imaginary part of the interband beat frequency $\omega = \Delta E/\hbar$ as a function of the dimensionless scaling parameter A.

As illustrated in Fig. 9(a), operating within the weak-dissipation perturbative limit ($A \leq 10^{-2}$), the higher-

order frequency shift induced by the $m^2\kappa^2$ term remains negligible. Therefore, the intrinsic interband beat frequency remains fundamentally unchanged, validating the utilization of the unperturbed interband frequency in our short-time dynamical analysis.

Acknowledgments

This work was supported by the National Key R & D Program of China under grants Nos. 2024YFF0726700, 2021YFA1400900, 2021YFA0718300, NSFC under grants Nos. 12334012, 12234012, 52327808, Space Application System of China Manned Space Program, Elite Revitalizing Inner Mongolia Program (2025TGL05).

References

[1] Schr"odinger E and Wiss S P A 1930 *Phys. Math. Kl.* **24** 418

[2] Schliemann J, Loss D and Westervelt R M 2005 *Phys. Rev. Lett.* **94** 206801

[3] Zawadzki W 2005 *Phys. Rev. B* **72** 085217

[4] Demikhovskii V Y, Maksimova G M and Frolova E V 2008 *Phys. Rev. B* **78** 115401

[5] Zawadzki W and Rusin T M 2011 *J. Phys.: Condens. Matter* **23** 143201

[6] Biswas T and Ghosh T K 2012 *J. Phys.: Condens. Matter* **24** 185304

[7] Cunha S M, da Costa D R, de Sousa G O, Chaves A, Pereira J M and Farias G A 2019 *Phys. Rev. B* **99** 235424

[8] Sedov E S, Sedova I E, Arakelian S M and Kavokin A V 2020 *New J. Phys.* **22** 083059

[9] Lovett S, Walker P M, Osipov A, Yulin A, Naik P U, Whittaker C E, Shelykh I A, Skolnick M S and Krizhanovskii D N 2023 *Light Sci. Appl.* **12** 126

[10] Vaishnav J Y and Clark C W 2008 *Phys. Rev. Lett.* **100** 153002

[11] Zhang Y C, Song S W, Liu C F and Liu W M 2013 *Phys. Rev. A* **87** 023612

[12] Longhi S 2010 *Opt. Lett.* **35** 235

[13] Liu Z, Wei G, Zhang D, Chen W, Sun L, Li J and Xiao J J 2021 *Phys. Rev. B* **103** 195415

[14] Brusheim P and Xu H Q 2007 *Phys. Rev. B* **75** 195333

[15] D'avid G and Cserti J 2010 *Phys. Rev. B* **81** 121417

[16] Winkler R, Z"ulicke U and Bolte J 2007 *Phys. Rev. B* **75** 205314

[17] Schliemann J, Loss D and Westervelt R M 2006 *Phys. Rev. B* **73** 085323

[18] Jung E, Park D and Park C S 2013 *Phys. Rev. B* **87** 115438

[19] Leary C C and Smith K H 2014 *Phys. Rev. A* **89** 023831

[20] Zhang X 2008 *Phys. Rev. Lett.* **100** 113903

[21] Pedernales J S, Beau M, Pittman S M, Egusquiza I L, Lamata L, Solano E and del Campo A 2018 *Phys. Rev. Lett.* **120** 160403

[22] Lai Y, Zhang Y and Chang K 2025 *Phys. Rev. Lett.* **135** 233802

[23] Bender C M and Boettcher S 1998 *Phys. Rev. Lett.* **80** 5243

[24] Zhao X M, Guo C X, Kou S P, Zhuang L and Liu W M 2021 *Phys. Rev. B* **104** 205131

[25] Zhao X M, Guo C X, Yang M L, Wang H, Liu W M and Kou S P 2021 *Phys. Rev. B* **104** 214502

[26] Yu Z F, Xue J K, Zhuang L, Zhao J and Liu W M 2021 *Phys. Rev. B* **104** 235408

[27] Wang H Y and Liu W M 2022 *Phys. Rev. A* **106** 052216

[28] Li C, Wu Y and Liu W M 2024 *Phys. Rev. B* **109** 214306

[29] Chu Z, Cai M, Yu Y and Wang B 2025 *Phys. Rev. B* **111** 235446

[30] Wei M, Wang B and Wang J 2025 *Phys. Rev. B* **111** 075135

[31] Li Y, Lu J, Wang C and Jiang J H 2025 *Chin. Phys. Lett.* **42** 047303

[32] Cao K, Du Q and Kou S P 2023 *Phys. Rev. B* **108** 165420

[33] Yao S and Wang Z 2018 *Phys. Rev. Lett.* **121** 086803

[34] Wang X R, Guo C X and Kou S P 2020 *Phys. Rev. B* **101** 121116

[35] Guo C X, Wang X R, Wang C and Kou S P 2020 *Phys. Rev. B* **101** 144439

[36] Yang Z and Hu J 2019 *Phys. Rev. B* **99** 081102

[37] Ruan Y P, Tang J S, Li Z, Wu H, Zhou W, Xiao L, Chen J, Ge S J, Hu W, Zhang H, Qiu C W, Liu W, Jing H, Lu Y Q and Xia K 2025 *Nat. Photonics* **19** 109

[38] Ding K H, Zhuang L and Liu W M 2026 *Phys. Rev. B* **113** 035439

[39] Mostafazadeh A 2002 *J. Math. Phys.* **43** 205

[40] Wang G, Xu H, Huang L and Lai Y C 2017 *New J. Phys.* **19** 013017

[41] Zhang Q 2019 *Heliyon* **5** e01532

[42] Wang N, Zhang R Y, Chan C T and Wang G P 2020 *Phys. Rev. B* **102** 094312

[43] Uhdre G M, Cius D and Andrade F M 2022 *Phys. Rev. A* **105** 013703

[44] Ye W, Liu J, Gao Y and Zhang S 2022 *Phys. Rev. B* **106** L060303

[45] Cai W *et al.* 2022 *Opt. Express* **30** 46982

[46] Zhan K, Zhao T, Chen Q, Zhang Q and Kang X 2023 *Appl. Phys. Lett.* **123** 191107

[47] Hu Y M R, Ostrovskaya E A and Estrecho E 2025 *Appl. Phys. Lett.* **127** 253101

[48] Luttinger J M 1956 *Phys. Rev.* **102** 1030

[49] Jiang Z F, Li R D, Zhang S C and Liu W M 2005 *Phys. Rev. B* **72** 045201

[50] Shen S Q 2005 *Phys. Rev. Lett.* **95** 187203

[51] Ju C Y, Miranowicz A, Barnett J, Chen G Y and Nori F 2025 *Phys. Rev. A* **111** 052213

[52] Murakami S, Nagaosa N and Zhang S C 2003 *Science* **301** 1348

[53] Zürch M, Chang H T, Borja L J, Kraus P M, Cushing S K, Gandman A, Kaplan C J, Oh M H, Prell J S, Prendergast D, Pemmaraju C D, Neumark D M and Leone S R 2017 *Nature Communications* **8** 15734

[54] Woerner M, Elsaesser T and Kaiser W 1990 *Phys. Rev. B* **41** 5463(R)–5466(R)

[55] Elsaesser T, Woerner M, Portella M T, Frey W, Ludwig C and Lohner A 1994 *Semiconductor Science and Technology* **9** 689

[56] Gupta A, Gupta V, Bohus J, Chordiya K, Kahaly M U, Sharma A and Fülöp J A 2023 *48th International Conference on Infrared, Millimeter, and Terahertz Waves (IRMMW-THz)* 1–2